

# A Double-Sided *LC*-Compensation Circuit for Loosely Coupled Capacitive Power Transfer

Fei Lu<sup>1</sup>, Student Member, IEEE, Hua Zhang<sup>2</sup>, Student Member, IEEE, Heath Hofmann, Senior Member, IEEE, and Chunting Chris Mi<sup>3</sup>, Fellow, IEEE

**Abstract**—This paper proposes a double-sided *LC*-compensation circuit for a loosely coupled, long-distance capacitive power transfer (CPT) system. A CPT system usually contains two pairs of metal plates as the capacitive coupler. An *LC*-compensation circuit resonates with the coupler to generate high voltages, and corresponding electric fields, to transfer power. When the compensation circuit is used on both the primary and secondary sides, it results in a double-sided *LC*-compensated CPT system. The working principle and frequency properties of the CPT system are analyzed. The results show a similarity with the series-series-compensated inductive power transfer system, which has both constant-voltage (CV) and constant-current (CC) working modes. *LC*-compensation is also compared with *LCLC*-compensation in terms of power, frequency properties, and output efficiency. A 150-W double-sided *LC*-compensated CPT prototype is designed and implemented to demonstrate a loosely coupled CPT system with 2.16% coupling coefficient. For both CC and CV working modes, the experimental results achieve dc–dc efficiencies higher than 70% across an air-gap distance of 180 mm with a switching frequency of 1.5 MHz.

**Index Terms**—Capacitive power transfer (CPT), double-sided *LC* compensation, frequency property.

## I. INTRODUCTION

CAPACITIVE power transfer (CPT) technology utilizes multiple metal plates to transfer power without direct metal-to-metal contact via alternating electric fields [1], [2]. Since electric fields can experience metal objects without generating significant power losses, CPT can be used in areas where inductive power transfer (IPT) technology [3], [4] is not convenient.

Manuscript received November 21, 2016; revised January 17, 2017; accepted February 22, 2017. Date of publication February 24, 2017; date of current version November 2, 2017. This work was supported in part by the U.S. Department of Energy Graduate Automotive Technology Education Grant, in part by the San Diego State University, and in part by the University of Michigan–Ann Arbor. Recommended for publication by Associate Editor O. Trescases.

F. Lu is with the Electrical Engineering and Computer Science Department, University of Michigan, Ann Arbor, MI 48109 USA, and also with the Department of Electrical and Computer Engineering, San Diego State University, San Diego, CA 92182 USA (e-mail: feilu@umich.edu).

H. Zhang is with the Department of Electrical and Computer Engineering, San Diego State University, San Diego, CA 92182 USA, and also with the School of Automation, Northwestern Polytechnical University, Xi’an 710072, China (e-mail: hzhang@mail.sdsu.edu).

H. Hofmann is with the Electrical Engineering and Computer Science Department, University of Michigan, Ann Arbor, MI 48109 USA (e-mail: hofmann@umich.edu).

C. C. Mi is with the Department of Electrical and Computer Engineering, San Diego State University, San Diego, CA 92182 USA (e-mail: cmi@sdsu.edu).

Color versions of one or more of the figures in this paper are available online at <http://ieeexplore.ieee.org>.

Digital Object Identifier 10.1109/TPEL.2017.2674688

CPT technology has been widely used in short-distance applications, varying from mW to kW levels, including biomedical devices [5], [6], integrated circuits [7], LED drivers [8], and the excitation of a rotor field winding in synchronous machines [9]. The transfer distance is usually within the millimeter range, which results in a coupling capacitance of up to tens of nanofarad. When dielectric material is inserted between the coupler plates, the coupling capacitance is significantly increased [10], [11]. This has been used in a CPT system which charges an electric vehicle via the front bumper [12]. The advantage of short-distance CPT systems is that the electric field flux is confined between the metal plates, and the fringing effect of the electric fields is reduced. Therefore, the electric fields emitted to the nearby environment are limited, and it can be safely used in close proximity to living things.

Long-distance CPT technology, where the transfer distance can reach hundreds of millimeters, has not been well studied. It can be used in electric vehicle charging applications, where the vehicle is charged by a transmitter located underneath the vehicle. It can also be readily extended to dynamic charging, where the vehicle receives power while it is moving [13]. The wheels of the vehicle can also help to enhance the capacitive coupling, as the rubber tires can work as a dielectric material to increase the coupling capacitance [14].

The coupling capacitance in a long-distance CPT system is usually in the pF range, which requires either high frequency or high voltage for high power. The switching frequency can be tens to hundreds of MHz [15], [16]. The class-E converter is a good candidate to realize a high-frequency CPT system [17], [18]. However, the power of high-frequency converters is usually lower than the kW level, which limits the power of CPT systems.

Increasing the voltage across the coupling plates can increase system power levels. A straightforward method is to use a step-up transformer with a large turn ratio to boost the voltage on the plates [19]. An *LCL* network at the front end can also increase the voltage [20]. However, both of these topologies require a large series inductor to directly resonate with the small capacitor. To reduce the resonant inductance, large external capacitors are connected in parallel with the plates, which results in the *LCLC* [21]–[23] and *CLLC* [24]–compensation circuits. The voltage on the plates can then increase to the kilovolt level, and these CPT systems have been shown to achieve 2.4 kW power transfer across an air-gap distance of 150 mm with a dc–dc efficiency of 90.8% [21]. However, in this case

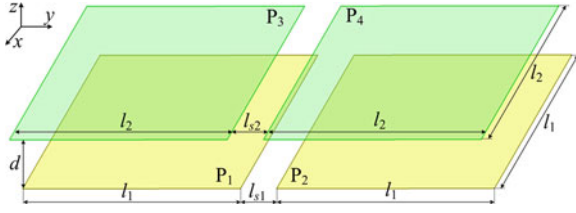


Fig. 1. Structure and dimensions of capacitive coupler.

TABLE I  
PARAMETER DESCRIPTION OF THE CAPACITIVE COUPLER

Parameter	Description	Parameter	Description
$l_1$	Primary plate length	$l_2$	secondary plate length
$l_{s1}$	Primary plate separation	$l_{s2}$	secondary plate separation
$d$	Primary–secondary gap	$t_p$	plate thickness

there are eight external components, which increase the system complexity.

A double-sided  $LC$ -compensation circuit topology is proposed in this paper to realize loosely coupled, long-distance CPT [25]. Compared to  $LCLC$  compensation, the number of external components is reduced. This circuit topology is derived from a series compensation circuit presented in [26]–[28], where two external inductors are connected to a capacitive coupler to create a resonance. In [26], there is no external capacitance connected to the capacitive coupler. As a result, the coupling coefficient is relatively high, and it is not a loosely coupled CPT system. Although the efficiency of the resonant tank reaches 83.6%, the system total dc–dc efficiency could be much lower due to power losses in the high-frequency (27.12 MHz) power amplifier. In this paper, an  $LC$ -compensated CPT system is excited by a full-bridge inverter, which is much easier to realize in practice. The frequency properties of the  $LC$ -compensated resonant circuit are studied to determine the relationship between the system power and circuit parameters. A loosely coupled CPT system with 2.16% coupling coefficient is designed and implemented based on the circuit analysis. Experimental results validate the proposed circuit topology. Finally, the  $LC$ - and  $LCLC$ -compensation circuits are compared in terms of power, frequency properties, and output efficiency.

## II. A DOUBLE-SIDED $LC$ -COMPENSATED CPT SYSTEM

### A. Capacitive Coupler

The capacitive coupler contains four metal plates, as shown in Fig. 1. Plates  $P_1$  and  $P_2$  are placed at the primary side as a power transmitter, while plates  $P_3$  and  $P_4$  are placed at the secondary side as a power receiver [21]. The dimensions of the plates are defined in Table I.

The circuit model of the capacitive coupler is shown in Fig. 2. There are capacitive couplings between every two plates, which results in six coupling capacitors. It is further simplified as a two-port model, in which  $C_{in1}$  and  $C_{in2}$  are the internal self-capacitances and  $C_M$  is the equivalent mutual capacitance [22].

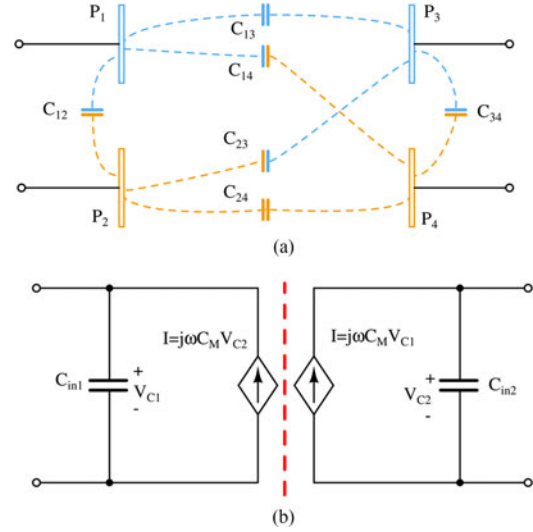
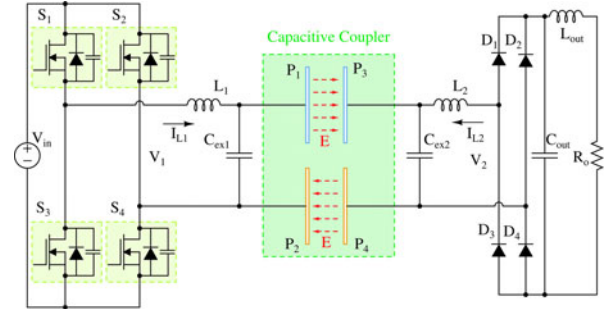


Fig. 2. Circuit model of capacitive coupler. (a) Full-capacitor model. (b) Equivalent two-port model.

Fig. 3. Circuit topology of a double-sided  $LC$ -compensated CPT system.

### B. Circuit Topology of $LC$ Compensation

Using the designed capacitive coupler, the circuit topology of a double-sided  $LC$ -compensated CPT system is shown in Fig. 3. External capacitors  $C_{ex1}$  and  $C_{ex2}$  are connected in parallel with the coupler to increase the equivalent self-capacitance. Inductors  $L_1$  and  $L_2$  resonate with the capacitor to produce high voltages. A full-bridge inverter is used to supply the ac excitation, and a full-bridge rectifier provides dc current to the load.

Using the two-port model in Fig. 2 to replace the capacitive coupler, an equivalent circuit model of the  $LC$ -compensated CPT system is shown in Fig. 4. The two voltage-dependent current sources represent the capacitive coupling between the primary and secondary. The equivalent self-capacitances are expressed as  $C_1 = C_{in1} + C_{ex1}$  and  $C_2 = C_{in2} + C_{ex2}$ , and the capacitive coupling coefficient is  $k_C = C_M / \sqrt{C_1 \cdot C_2}$ .

## III. WORKING PRINCIPLE OF DOUBLE-SIDED $LC$ -COMPENSATED CPT SYSTEM

### A. Output Properties

The fundamental harmonics approximation (FHA) method is used to analyze the circuit working principle, as shown in Fig. 5. The square-wave excitation provided by the full-bridge inverter is approximated by a pure sinusoidal input, and so high-

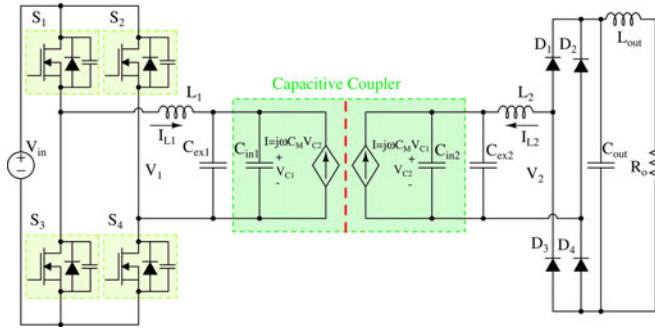


Fig. 4. Equivalent circuit topology of LC-compensated CPT system.

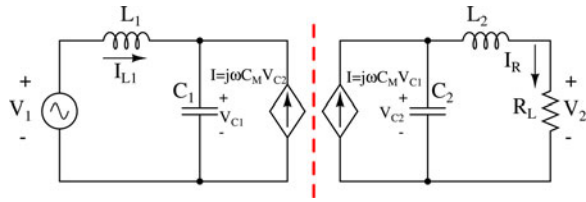


Fig. 5. FHA of LC-compensated CPT system.

 TABLE II  
 ADMITTANCES OF THE CIRCUIT COMPONENTS

Parameter	Expression	Parameter	Expression
$Y_{L1}$	$\frac{1}{j\omega L_1}$	$Y_{L2}$	$\frac{1}{j\omega L_2}$
$Y_{C1}$	$j\omega C_1$	$Y_{C2}$	$j\omega C_2$
$Y_1$	$j\omega C_1 + \frac{1}{j\omega L_1}$	$Y_2$	$j\omega C_2 + \frac{1}{j\omega L_2}$
$Y_M$	$j\omega C_M$	$Y_{RL}$	$\frac{1}{R_L}$

order harmonics are neglected. An equivalent load resistor  $R_L$  is used to represent the output resistor  $R_o$ , whose value is  $R_L = R_o \times 8/\pi^2$ .

Instead of impedances, admittances are used in the analysis, which are defined in Table II.

The KCL equations of Fig. 5 indicate that

$$\begin{cases} Y_{L1} \cdot (V_1 - V_{C1}) + Y_M \cdot V_{C2} = V_{C1} \cdot Y_1 \\ Y_{L2} \cdot (V_2 - V_{C2}) + Y_M \cdot V_{C1} = V_{C2} \cdot Y_2 \\ Y_{L2} \cdot (V_2 - V_{C2}) = -Y_{RL} \cdot V_2. \end{cases} \quad (1)$$

According to these equations, the voltage gain  $G_v$  between the input and output voltage is determined to be

$$G_v = \frac{V_2}{V_1} = \frac{Y_{L1} \cdot Y_{L2} \cdot Y_M}{(Y_1 Y_2 - Y_M^2)/R_L + Y_{L2} \cdot (Y_1 Y_2 - Y_M^2 - Y_1 Y_{L2})}. \quad (2)$$

Since a resistive load is used on the output side, the transconductance  $G_i$  is further expressed as

$$G_i = \frac{I_R}{V_1} = \frac{Y_{L1} \cdot Y_{L2} \cdot Y_M}{(Y_1 Y_2 - Y_M^2) + Y_{L2} \cdot (Y_1 Y_2 - Y_M^2 - Y_1 Y_{L2}) \cdot R_L}. \quad (3)$$

The expressions (2) and (3) show that the output voltage  $V_2$  and current  $I_R$  relate to the admittances of the passive components and the load resistance  $R_L$ . These two expressions will be

used to analyze the system frequency properties, which result in constant-voltage (CV) and constant-current (CC) working modes.

### B. CV Working Mode

According to (2), the CV condition is determined by taking  $dG_v/dR_L = 0$ , which results in

$$Y_1 Y_2 - Y_M^2 = 0. \quad (4)$$

By defining the self-resonant frequencies as

$$\omega_1 = \frac{1}{\sqrt{L_1 \cdot C_1}}, \quad \omega_2 = \frac{1}{\sqrt{L_2 \cdot C_2}} \quad (5)$$

the CV frequencies can be expressed as follows:

$$\omega_{v1,2} = \sqrt{\frac{(\omega_1^2 + \omega_2^2) \mp \sqrt{(\omega_1^2 - \omega_2^2)^2 + 4 \cdot k_C^2 \cdot \omega_1^2 \omega_2^2}}{2 \cdot (1 - k_C^2)}}. \quad (6)$$

The magnitude of  $G_v$  at these frequencies is therefore

$$|G_v|_{\omega=\omega_{v1,2}} = \left| \frac{V_2}{V_1} \right| = \sqrt{\frac{\omega_{v1,2}^2 - \omega_2^2}{\omega_{v1,2}^2 - \omega_1^2}} \cdot \frac{\omega_1^2}{\omega_2^2} \cdot \sqrt{\frac{C_1}{C_2}}. \quad (7)$$

If the self-resonant frequencies at the primary and secondary sides are designed to be the same (i.e.,  $\omega_0 = \omega_1 = \omega_2$ ), then the CV frequencies are simplified as follows:

$$\begin{cases} \omega_{v1} = \frac{1}{\sqrt{1 + k_C}} \cdot \omega_0 \\ \omega_{v2} = \frac{1}{\sqrt{1 - k_C}} \cdot \omega_0 \end{cases}. \quad (8)$$

The magnitude of the voltage gain  $G_v$  at these frequencies is further simplified as

$$|G_v|_{\omega=\omega_{v1,2}} = \left| \frac{V_2}{V_1} \right| = \sqrt{\frac{C_1}{C_2}}. \quad (9)$$

When the self-capacitances  $C_1$  and  $C_2$  are equal, the magnitude of the input and output voltage are therefore also equal.

### C. CC Working Mode

Using (3), the CC frequency is determined by taking  $dG_i/dR_L = 0$ , which results in

$$Y_1 Y_2 - Y_M^2 - Y_1 Y_{L2} = 0. \quad (10)$$

Similar to the CV analysis, the CC frequency is given by

$$\omega_c = \frac{\omega_1}{\sqrt{1 - k_C^2}} \quad (11)$$

and the transconductance  $G_i$  at this frequency is as follows:

$$G_i|_{\omega=\omega_c} = \frac{I_R}{V_1} = \frac{-j\omega_c \cdot C_M \cdot (1 - k_C^2)}{k_C^2}. \quad (12)$$

In CC mode, the output current can be increased by decreasing  $k_C$ . However, it needs to be emphasized that the minimum  $k_C$  is limited by the voltage and current ratings of the circuit components, and the system efficiency decreases with decreasing  $k_C$ .

TABLE III  
OUTPUT VOLTAGE, CURRENT, AND POWER OF THE LC-COMPENSATED CPT SYSTEM, WHEN  $\omega_0 = \omega_1 = \omega_2$

Parameters	Conditions	$\omega_{v1,2} = \frac{\omega_0}{\sqrt{1 \pm k_C}}$	$\omega_c = \frac{\omega_0}{\sqrt{1 - k_C^2}}$
$ V_2 $		$ V_1  \cdot \sqrt{\frac{C_1}{C_2}}$	$ V_1  \cdot \frac{\omega_c \cdot C_M}{k_C^2} \cdot (1 - k_C^2) \cdot R_L$
$ I_R $		$\frac{ V_1 }{R_L} \cdot \sqrt{\frac{C_1}{C_2}}$	$ V_1  \cdot \frac{\omega_c \cdot C_M}{k_C^2} \cdot (1 - k_C^2)$
$P_{out} =  V_2  \cdot  I_R $		$\frac{ V_1 ^2}{R_L} \cdot \frac{C_1}{C_2}$	$ V_1 ^2 \cdot \left[ \frac{\omega_c \cdot C_M}{k_C^2} \cdot (1 - k_C^2) \right]^2 \cdot R_L$

TABLE IV  
SYSTEM SPECIFICATIONS AND CIRCUIT PARAMETERS OF A DOUBLE-SIDED LC-COMPENSATED CPT SYSTEM

Parameter	Design value	Parameter	Design value
$V_{in}$	0–64 V	$R_L$	20–40 $\Omega$
$l_1 (l_2)$	300 mm	$l_{s1} (l_{s2})$	150 mm
$d$	180 mm	$C_{in1} (C_{in2})$	9.8 pF
$C_M$	2.8 pF	$C_{ex1} (C_{ex2})$	120 pF
$k_C$	2.16%	$C_1 (C_2)$	129.8 pF
$f_0$	1.5 MHz	$L_1 (L_2)$	86.8 $\mu$ H

When  $\omega_0 = \omega_1 = \omega_2$ , the output voltage, current, and power of the LC-compensated CPT system at the CV and CC frequencies are expressed as in Table III.

#### IV. DESIGN OF A LOOSELY COUPLED CPT SYSTEMS

##### A. Circuit Parameters

A loosely coupled CPT system is designed in this section. To simplify the process, the capacitive coupler is designed to be symmetric, and the dimensions are determined as  $l_1 = l_2 = 300$  mm,  $l_{s1} = l_{s2} = 150$  mm,  $d = 180$  mm, and  $t_p = 2$  mm. Finite element analysis by Maxwell is further used to simulate the coupling capacitances between the plates. As shown in [22], the equivalent capacitances in Fig. 2(b) are calculated to be  $C_{in1} = C_{in2} = 9.8$  pF and  $C_M = 2.8$  pF.

According to the resonance relationships in (5) and admittances in Table III, the circuit parameters of the CPT system are designed as shown in Table IV. The parameters are symmetric from the primary to secondary side. The range of the input dc voltage is 0–64 V, and the output load resistance varies between 20 and 45  $\Omega$ . The resonant frequency  $f_0$  ( $f_0 = \omega_0/2\pi$ ) is set to 1.5 MHz. The external capacitors  $C_{ex1}$  and  $C_{ex2}$  are both 120 pF, which results in a coupling coefficient of 2.16%.

##### B. Frequency Properties

According to the analysis in Section III, the frequency properties of the designed loosely coupled LC-compensated CPT system are shown in Fig. 6. When the load resistance  $R_L$  varies, Fig. 6(a) shows that there are two CV frequencies,  $\omega_{v1}$  and  $\omega_{v2}$ , and Fig. 6(b) shows that there is a CC frequency  $\omega_c$ . It also

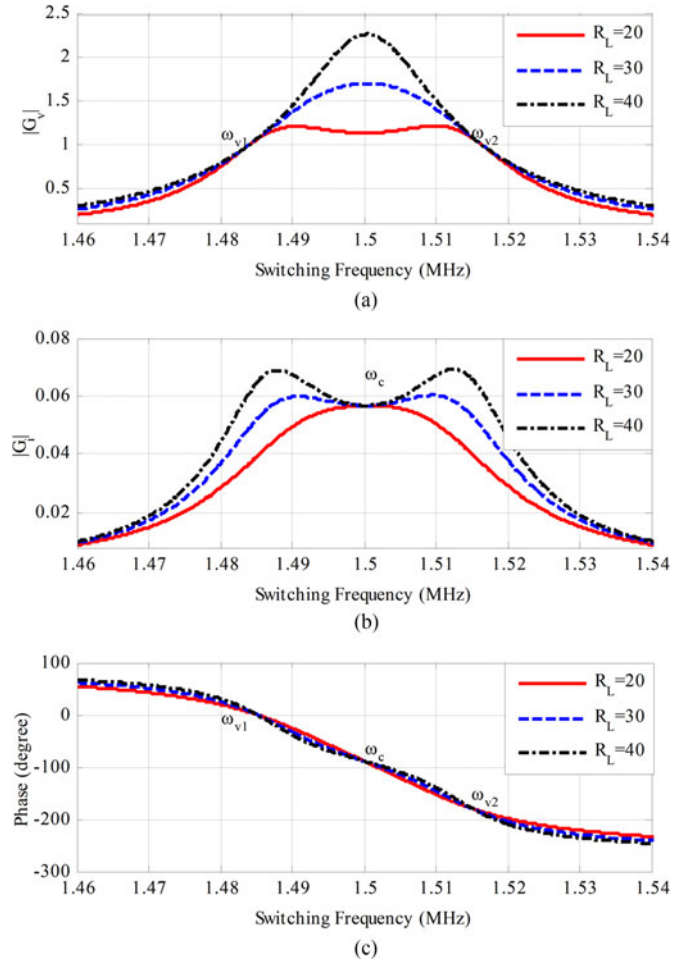


Fig. 6. Frequency properties of a loosely coupled double-sided LC-compensated CPT system with 2.16% coupling coefficient. (a) Magnitude of voltage gain  $G_v$ . (b) Magnitude of transconductance  $G_i$ . (c) Phase angle  $\theta$  of  $G_v$  and  $G_i$ .

shows that the CV gain is 1.0, and the CC frequency is between the two CV frequencies.

Fig. 6(c) shows the phase angle of  $G_v$  and  $G_i$  at different load conditions. The input ac voltage  $V_1$  is set as a reference. It is seen that the phases at the three special frequencies are  $\theta(\omega = \omega_{v1}) = 0^\circ$ ,  $\theta(\omega = \omega_c) = -90^\circ$ , and  $\theta(\omega = \omega_{v2}) = -180^\circ$ . Fig. 6 shows that the frequency properties of the double-sided LC-compensated CPT system are similar to the frequency properties of the series-series (SS) compensated IPT system [29].

##### C. Electric Field Emission

Using the circuit parameters in Table IV, the circuit performance is simulated using LTspice in the CC working condition. The rms value of the voltages across the circuit components and between the metal plates are shown in Table V.

It shows that the rms value of voltage between  $P_1$  and  $P_2$  is as high as 2.51 kV, and the voltage between  $P_1$  and  $P_3$  is 1.73 kV. Since the breakdown voltage of air is about 3 kV/mm and the distance between the plates is large sufficiently, there is no con-

TABLE V  
RMS VALUES OF THE VOLTAGES OF CIRCUIT COMPONENTS AND PLATES IN THE CC CONDITION

Parameter	Voltage	Parameter	Voltage
$V_{L1}$	2.50 kV	$V_{L2}$	2.50 kV
$V_{P1-P2}$	2.51 kV	$V_{P3-P4}$	2.51 kV
$V_{P1-P3}$	1.73 kV	$V_{P2-P4}$	1.73 kV

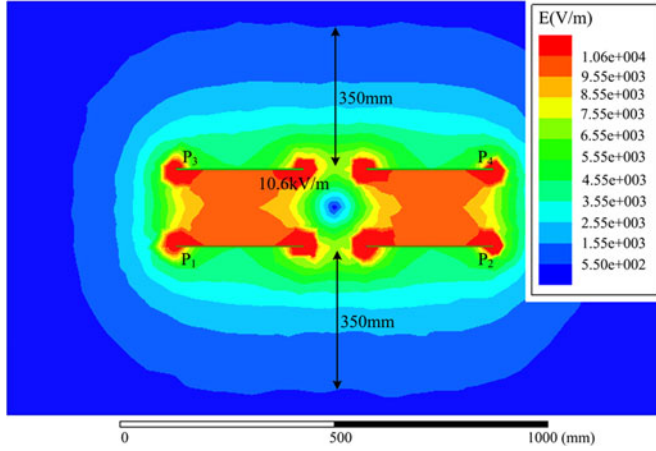


Fig. 7. Electric fields emission around the capacitive coupler.

cern with arcing in this system. As the coupling capacitance is only 2.8 pF and the coupling coefficient is only 2.16%, the compensation circuit is necessary in order to increase the plate voltages to kilovolt to achieve sufficient power transfer. Using the voltages in Table V, Maxwell is used to simulate the electric field emission around the capacitive coupler shown in Fig. 7.

Fig. 7 shows that the electric field strength between plates  $P_1$  and  $P_3$  is about 9.6 kV/m, and the maximum field strength close to the plates is about 10.6 kV/m. The IEEE C95.1 standard [30] requires that the electric field strength should be lower than 550 V/m at 1.5 MHz for human safety consideration. Therefore, Fig. 7 shows that the safe area being about 350 mm away from the coupler in this system.

In this CPT system, if the electric field strength between  $P_1$  and  $P_3$  were limited below the safety requirement, the plate voltages  $V_{P1-P3}$  and  $V_{P2-P4}$  would be reduced from 1.73 to 0.1 kV. The plate voltages  $V_{P1-P2}$  and  $V_{P3-P4}$  would then be limited to 0.14 kV. According to [31], the maximum achievable power is estimated as

$$P_{\max} = \omega_c C_M V_{P1-P2} V_{P3-P4} = 0.51 \text{ W}. \quad (13)$$

In a practical application, the electric fields between  $P_1$  and  $P_3$  have to be much larger than the safety limitation to transfer sufficient power. Therefore, a living object detection system should be used to protect human and animal safety, which is similar to the protection mechanism required in an IPT system. In future research, the shielding of leakage electric fields will also be studied to reduce the electric field emissions and hence increase the safety of the CPT system.

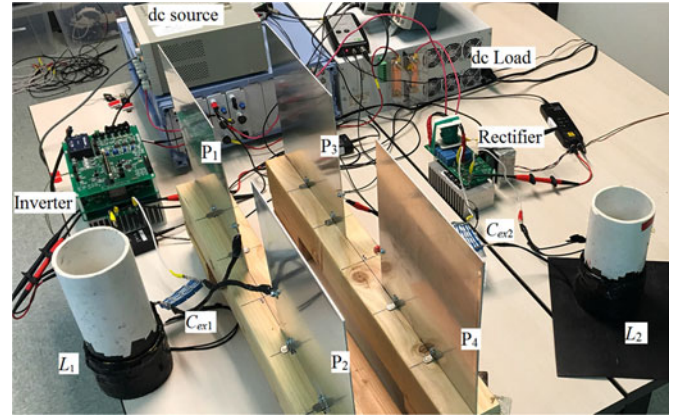


Fig. 8. Prototype of a double-sided LC-compensated CPT system.

## V. EXPERIMENTS

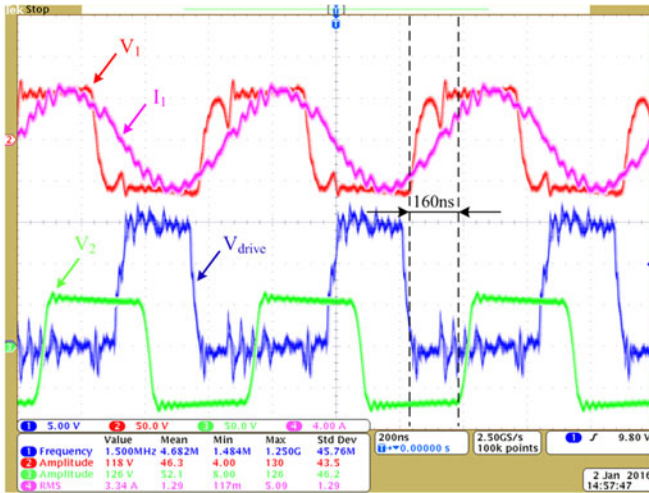
### A. Experimental Prototype

With all the circuit parameters provided in Table IV, an experimental prototype of the LC-compensated CPT system is implemented as shown in Fig. 8. Four aluminum plates form the capacitive coupler and are placed on a fixture made from wood. The plate length is 300 mm, and the air-gap distance is 180 mm to realize a loosely coupled system. The external parallel-connected capacitors  $C_{ex1}$  and  $C_{ex2}$  are high-frequency thin-film capacitors. The inductors  $L_1$  and  $L_2$  have an air core and are made with AWG 46 Litz-wire, thereby reducing both the skin-effect loss and magnetic loss. These inductors resonate with the capacitances to generate high voltages on the plates and transfer power. Since the switching frequency is 1.5 MHz, silicon carbide (SiC) mosfets are used in the input inverter, and SiC diodes are used in the output rectifier. A dc supply is connected to the inverter as the power source, and an electronic dc load is connected to the rectifier as the output. The load is set to resistive mode for both the CV and CC working conditions. The measurement of efficiency is from the dc source to the dc load.

### B. CC Mode Experiment

Using the designed prototype, experiments are conducted for both CC and CV working modes. The CC mode is investigated first. In this case, the inductor  $L_2$  is tuned to 86.1  $\mu\text{H}$  in order to achieve CC operation at 1.5 MHz and realize soft switching of the mosfets. The microcontroller TMS320F28335 from Texas Instruments is used to generate the pulse width modulation (PWM) signals for the input inverter. The switching frequency is set to be 1.5 MHz, and the dead time for the full-bridge inverter is approximately 80 ns. Experimental results of the CC mode are shown in Fig. 9 for a load resistance  $R_o = 33.1 \Omega$  ( $R_L = 26.8 \Omega$ ).

Fig. 9(a) shows the input and output waveforms of the CC working mode. The input current  $I_{L1}$  is slightly lagging the input voltage  $V_1$  to achieve soft switching of the MOSFETs. It also shows that the output voltage  $V_2$  is lagging the input voltage



(a)

Udc2	$V_{in}$	59.55 V	Udc3	$V_{out}$	61.01 V
I dc2		2.6754 A	I dc3		1.8411 A
P2	$P_{in}$	0.1593 kW	P3	$P_{out}$	0.1124 kW
S2		0.1602 kVA	S3		0.1125 kVA
Q2		-0.0167 kvar	Q3		-0.0041 kvar
Eff	$\eta$	70.567 %	Ploss		46.886 W
$\lambda$ 2		0.9946	U <sub>pk</sub> 2		61.63 V
Req2		22.147 ohm	Req3		33.117 ohm

(b)

Fig. 9. Experimental results of the CC working mode, when  $R_O = 33.1 \Omega$ . (a) Input and output waveforms. (b) Power and efficiency.

$V_1$  by about 160 ns. Since the switching frequency is 1.5 MHz, and the corresponding period is about 666.6 ns, this agrees with Fig. 6(c), which shows the output voltage  $V_2$  should lag the input voltage  $V_1$  by  $90^\circ$ . The driver signal  $V_{drive}$  of a mosfet is also provided in Fig. 9(a). Although there is some noise in the gate drive voltage, the noise magnitude is lower than the threshold voltage of the MOSFET, which is acceptable for driving the devices.

Fig. 9(b) shows the system measurements. When the input dc voltage is 59.5 V, the output load resistance is tuned to  $33 \Omega$  to achieve an output voltage of 61 V. In this case, the input power is 159.3 W, and the output power is 112.4 W, resulting in a power loss of 46.9 W and a dc–dc efficiency of 70.6%.

The power loss distribution among the circuit components is shown in Fig. 10. The power loss in the compensation inductors, capacitors, MOSFETs, and diodes can be calculated by their inner resistances from the datasheets and measurements [4]. The remaining losses are assumed to be in the plates. Fig. 10 shows that the compensation capacitors  $C_1$  and  $C_2$  dissipate approximately 40% of the power loss. In future designs, better film

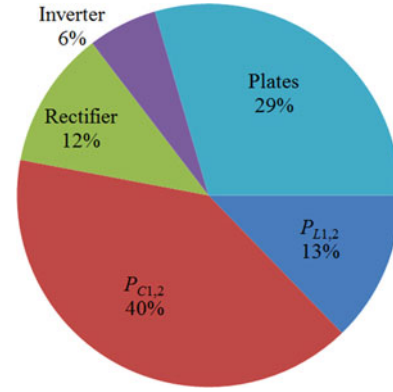


Fig. 10. Power loss distribution among circuit components in CC condition.

capacitors with a lower dissipation factor can be used to reduce the system loss and improve its efficiency.

### C. CV Mode Experiment

The ePWM module of TMS320F28335 is used to generate PWM signals. Since the CPU speed is 150 MHz, the frequency resolution of the PWM signal is 30 kHz at 1.5 MHz. According to Fig. 6, the bandwidth of the system is very small, and it is therefore difficult to achieve the CV mode by tuning the switching frequency. Therefore, both the inductors  $L_1$  and  $L_2$  are tuned to  $88.5 \mu\text{H}$  to achieve CV operation at 1.5 MHz. The experimental results of the CV working mode are shown in Fig. 11 for a load resistance  $R_o = 44 \Omega$  ( $R_L = 35.7 \Omega$ ).

Once again, the input current  $I_{L1}$  is slightly lagging the input voltage  $V_1$  to achieve soft switching of the MOSFETs. The output current  $I_R$  is in phase with the output voltage  $V_2$  at the rectifier side. It is also seen that the output voltage  $V_2$  is lagging the input voltage  $V_1$  by about 330 ns, which agrees with the analysis in Fig. 6 that  $V_2$  is lagging  $V_1$  by  $180^\circ$  at the CV frequency  $\omega_{v2}$ .

Fig. 11(b) shows the system measurements. When the input voltage is 64.1 V, the output load resistance is tuned to  $44 \Omega$  to achieve an output voltage of 69.3 V. In this case, the input power is 146.2 W, and the output power is 109.3 W, resulting in a dc–dc efficiency of 74.8%. Because the CV mode has higher voltages and lower currents than the CC mode, the system efficiency is higher.

## VI. DISCUSSION: COMPARISON BETWEEN LC AND LCLC COMPENSATION

### A. Output Power Property

The LC-, LCLC- [21], and CLLC-compensation [24] topologies can achieve significant CPT. Compared to LCLC compensation, the CLLC compensation can slightly reduce the size of the compensation inductors  $L_1$  and  $L_2$ , but the system efficiency property is almost the same. Therefore, in this paper, LCLC compensation is used as a comparison to LC compensation, and the circuit topology is shown in Fig. 12.

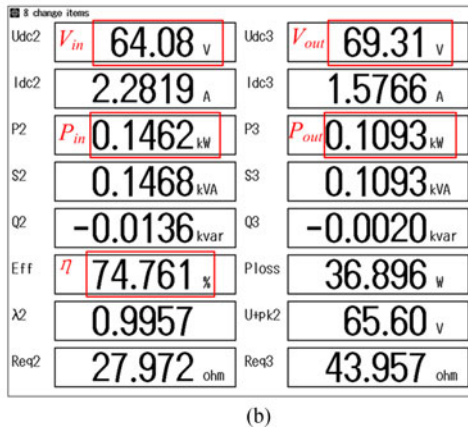
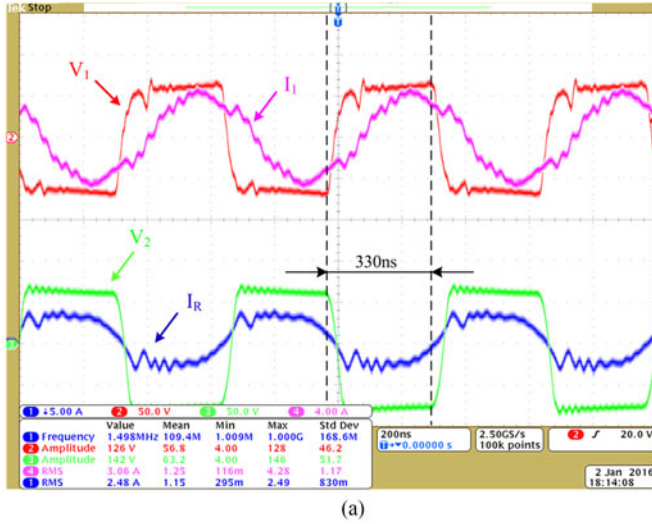


Fig. 11. Experimental results of the CV working mode, when  $R_O = 44 \Omega$ . (a) Input and output waveforms. (b) Power and efficiency.

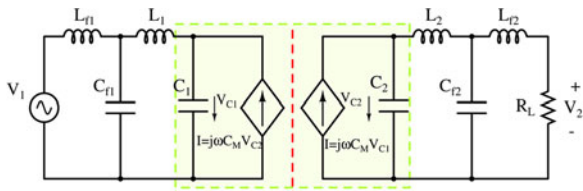


Fig. 12. Circuit topology of a double-sided LCLC-compensated CPT system.

In CC mode, the output power of LC- and LCLC-compensated [21] systems is expressed as

$$\begin{cases} P_{LC} = \omega_c \cdot C_M \cdot \frac{1}{k_C^2} \cdot V_1 \cdot V_2 \\ P_{LCLC} = \omega_c \cdot C_M \cdot \frac{C_{f1} C_{f2}}{C_1 C_2} \cdot V_1 \cdot V_2. \end{cases} \quad (14)$$

In the LC-compensated CPT system, as long as the mutual capacitance  $C_M$  is fixed, the output power is determined by the coupling coefficient  $k_C$ . Increasing power requires decreasing  $k_C$ , which reduces the system efficiency, as will be shown in the sequel. In an LCLC-compensated CPT system, the output power can be regulated by adjusting the ratio between  $C_{f1} C_{f2}$

TABLE VI  
SYSTEM SPECIFICATIONS AND CIRCUIT PARAMETERS OF A DOUBLE-SIDED LCLC-COMPENSATED CPT SYSTEM

Parameter	Design value	Parameter	Design value
$V_{in}$	0–64 V	$R_L$	20–40 $\Omega$
$l_1$ ( $l_2$ )	300 mm	$l_{s1}$ ( $l_{s2}$ )	150 mm
$d$	180 mm	$C_{in1}$ ( $C_{in2}$ )	9.8 pF
$C_M$	2.8 pF	$C_{ex1}$ ( $C_{ex2}$ )	46 pF
$k_C$	5.0%	$C_1$ ( $C_2$ )	55.8 pF
$C_{f1}$ ( $C_{f2}$ )	2.72 nF	$L_{f1}$ ( $L_{f2}$ )	4.14 $\mu$ H
$f_0$	1.5 MHz	$L_1$ ( $L_2$ )	196.0 $\mu$ H

and  $C_1 C_2$ . This provides the flexibility to design the capacitive coupler to achieve a relatively large coupling coefficient  $k_C$ , which results in a better system efficiency.

### B. Frequency Property

As seen in Fig. 6, the working bandwidth of the LC-compensated CPT system is narrow, and the system power drops quickly when the switching frequency moves away from the resonance frequency. As a comparison, an LCLC-compensated CPT system is designed to transfer the same power using the same capacitive coupler, except that the coupling coefficient is higher at 5%. The circuit parameters are designed according to [21], as shown in Table VI.

The frequency properties of the LCLC-compensated CPT system are shown in Fig. 13. Since the coupling coefficient  $k_C$  is larger than the LC-compensated CPT system, the operating bandwidth is significantly increased. The magnitudes of  $|G_i|$  and  $|G_v|$  are therefore less sensitive to variations in the switching frequency. It is also seen that a CC mode exists at the resonant frequency, and the phase angle of  $G_v$  and  $G_i$  is  $90^\circ$  leading  $V_1$ .

### C. System Efficiency

The efficiency of the LC-compensated CPT network (i.e. not including inverter and rectifier losses) is expressed as

$$\eta_{LC} = \frac{I_{RL}^2 \cdot R_L}{I_{RL}^2 \cdot R_L + I_{L2}^2 \cdot R_{L2} + I_{C2}^2 \cdot R_{C2} + I_{C1}^2 \cdot R_{C1} + I_{L1}^2 \cdot R_{L1}} \quad (15)$$

where  $R_{L2}$ ,  $R_{C2}$ ,  $R_{C1}$ , and  $R_{L1}$  are the parasitic resistances of the passive components, and  $I_{RL}$ ,  $I_{L2}$ ,  $I_{C2}$ ,  $I_{C1}$ , and  $I_{L1}$  are the currents flowing through these components. The efficiency can be rewritten as

$$\eta_{LC} = \frac{1}{1 + \left| \frac{I_{L2}}{I_{RL}} \right|^2 \cdot \frac{R_{L2}}{R_L} + \left| \frac{I_{C2}}{I_{RL}} \right|^2 \cdot \frac{R_{C2}}{R_L} + \left| \frac{I_{C1}}{I_{RL}} \right|^2 \cdot \frac{R_{C1}}{R_L} + \left| \frac{I_{L1}}{I_{RL}} \right|^2 \cdot \frac{R_{L1}}{R_L}} \quad (16)$$

The magnitudes of the current ratios can be approximated using the FHA. At the CC frequency, the efficiency can be

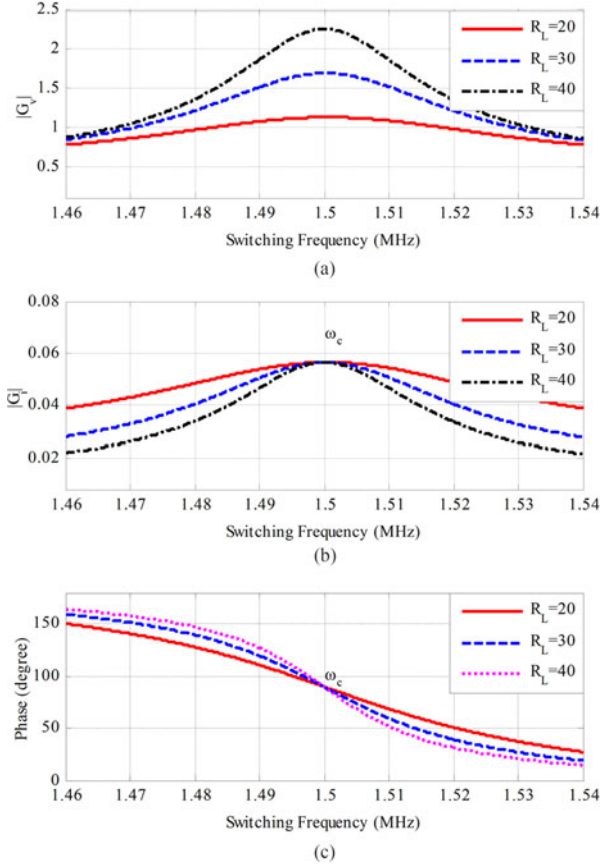


Fig. 13. Frequency property of a double-sided *LCLC*-compensated CPT system with 5% coupling coefficient. (a) Magnitude of voltage gain  $G_v$ . (b) Magnitude of transconductance  $G_i$ . (c) Phase angle  $\theta$  of  $G_v$  and  $G_i$ .

expressed as follows:

$$\eta_{LC} = \frac{1}{1 + \frac{2}{k_C^2 Q_1 Q_2} + \frac{1}{\alpha k_C^2 Q_1 Q_2} + \left(1 + \frac{1}{k^2 Q_1 Q_2}\right) \alpha} \quad (17)$$

where  $Q_1$  and  $Q_2$  are the quality factors of the primary and secondary resonant circuits, given as follows:

$$\begin{cases} R_1 = R_{L1} + R_{C1}, R_2 = R_{L2} + R_{C2} \\ Q_1 = 1/(\omega C_1 R_1), Q_2 = 1/(\omega C_2 R_2) \\ \alpha = R_2/R_L. \end{cases} \quad (18)$$

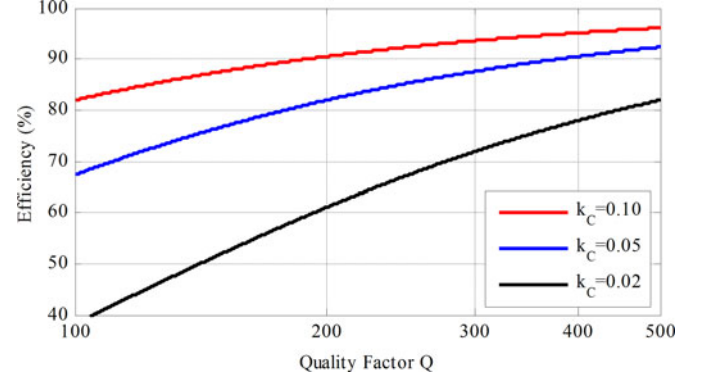


Fig. 14. Theoretical maximum achievable efficiency of a double-sided *LC*-compensated CPT network.

It can be further shown that the load resistance that maximizes efficiency is given by

$$R_L = \sqrt{1 + k_C^2 Q_1 Q_2} \cdot R_2 \quad (19)$$

and the resulting efficiency is expressed as

$$\eta_{LC, \max} = \frac{1}{1 + \frac{2}{k_C^2 Q_1 Q_2} + \frac{2}{\sqrt{k_C^2 Q_1 Q_2}} \sqrt{\left(1 + \frac{1}{k_C^2 Q_1 Q_2}\right)}} \quad (20)$$

To simplify analysis, the quality factor is assumed to be equal for the primary and secondary (i.e.,  $Q = Q_1 = Q_2$ ). The maximum efficiency is then further simplified as

$$\eta_{LC, \max} = \frac{1}{1 + \frac{2}{k_C^2 Q^2} + \frac{2}{k_C Q} \sqrt{\left(1 + \frac{1}{k_C Q}\right)}} \quad (21)$$

The theoretical maximum achievable efficiency of the *LC*-compensated CPT network is shown in Fig. 14 as a function of quality factor and coupling coefficient. It is seen that the efficiency increases with the increasing quality factor  $Q$  and coupling coefficient  $k_C$ . It is similar to the efficiency of the *SS*-compensated IPT system [31] shown in (22) and (23) at the bottom of this page.

Fig. 12 is used to analyze the efficiency of the *LCLC*-compensated CPT network, expressed as (22). The efficiency is further rewritten as (23).

$\eta_{LCLC}$

$$= \frac{I_{RL}^2 \cdot R_L}{I_{RL}^2 \cdot R_L + I_{Lf2}^2 \cdot R_{Lf2} + I_{Cf2}^2 \cdot R_{Cf2} + I_{L2}^2 \cdot R_{L2} + I_{C2}^2 \cdot R_{C2} + I_{C1}^2 \cdot R_{C1} + I_{L1}^2 \cdot R_{L1} + I_{Cf1}^2 \cdot R_{Cf1} + I_{Lf1}^2 \cdot R_{Lf1}} \quad (22)$$

$\eta_{LCLC}$

$$= \frac{1}{1 + \left|\frac{I_{Lf2}}{I_{RL}}\right|^2 \frac{R_{Lf2}}{R_L} + \left|\frac{I_{Lf2}}{I_{RL}}\right|^2 \frac{R_{Cf2}}{R_L} + \left|\frac{I_{Lf2}}{I_{RL}}\right|^2 \frac{R_{L2}}{R_L} + \left|\frac{I_{Lf2}}{I_{RL}}\right|^2 \frac{R_{C2}}{R_L} + \left|\frac{I_{Lf2}}{I_{RL}}\right|^2 \frac{R_{C1}}{R_L} + \left|\frac{I_{Lf2}}{I_{RL}}\right|^2 \frac{R_{L1}}{R_L} + \left|\frac{I_{Lf2}}{I_{RL}}\right|^2 \frac{R_{Cf1}}{R_L} + \left|\frac{I_{Lf2}}{I_{RL}}\right|^2 \frac{R_{Lf1}}{R_L}} \quad (23)$$

Similarly, the magnitudes of the current ratios in the denominator can be derived using fundamental harmonics analysis. At the CC frequency [23], the efficiency can be simplified and expressed as

$$\eta_{LCLC} = \frac{1}{1 + \frac{1}{\alpha\gamma Q_1 Q_2 \beta_1 \beta_2^2} \left( \frac{Q_2}{Q_{f1}} k_C^2 + \beta_1 \right) + \frac{\gamma\beta_2}{k_C^2} \left( \frac{Q_1}{Q_{f2}} k_C^2 + \beta_2 \right)} \alpha \quad (24)$$

where

$$\begin{cases} R_{f1} = R_{L_{f1}} + R_{C_{f1}}, R_{f2} = R_{L_{f2}} + R_{C_{f2}} \\ Q_{f1} = 1/(\omega C_{f1} R_{f1}), Q_{f2} = 1/(\omega C_{f2} R_{f2}) \\ R_1 = R_{L_1} + R_{C_1} + R_{C_{f1}}, R_2 = R_{L_2} + R_{C_2} + R_{C_{f2}} \\ Q_1 = 1/(\omega C_1 R_1), Q_2 = 1/(\omega C_2 R_2) \\ \alpha = R_2/R_{L_1}, \gamma = C_1/C_2 \\ \beta_1 = C_1/C_{f1}, \beta_2 = C_2/C_{f2}. \end{cases} \quad (25)$$

The efficiency is maximized when the load resistance is

$$R_L = \frac{\gamma\sqrt{\beta_1\beta_2^3}\sqrt{Q_1Q_2}}{k} \cdot \frac{\sqrt{\beta_1 + k_C^2 Q_2/Q_{f1}}}{\sqrt{\beta_2 + k_C^2 Q_1/Q_{f2}}} \cdot R_2 \quad (26)$$

resulting in the following efficiency:

$$\eta_{LCLC,max} = \frac{1}{1 + \frac{2}{k_C\sqrt{Q_1Q_2}} \cdot \sqrt{\left(1 + \frac{Q_2}{Q_{f1}} \cdot \frac{k_C^2}{\beta_1}\right) \cdot \left(1 + \frac{Q_1}{Q_{f2}} \cdot \frac{k_C^2}{\beta_2}\right)}} \quad (27)$$

To simplify the analysis, the circuit is assumed to be symmetric, which results in  $Q_{f1} = Q_{f2}$  and  $Q_1 = Q_2$ . In this system,  $Q_{f1}$  represents the quality factor of a resonant circuit including  $L_{f1}$  and  $C_{f1}$ , and  $Q_1$  represents the quality factor of a resonant circuit including  $L_1$ ,  $C_1$ , and  $C_{f1}$ . The inductors  $L_{f1}$  and  $L_1$  can be designed to have air core in order to achieve a high quality factor. Also, the same film capacitors can be used to build  $C_{f1}$  and  $C_1$ . Therefore, it can be assumed that  $Q_{f1} = Q_1$  to simplify the efficiency analysis. Further assumptions are shown as follows:

$$\begin{cases} Q = Q_1 = Q_2 = Q_{f1} = Q_{f2} \\ \beta = \beta_1 = \beta_2, \gamma = 1 \end{cases} \quad (28)$$

Therefore, the maximum efficiency of the *LCLC*-compensated system can be further simplified as

$$\eta_{LCLC,max} = \frac{1}{1 + \frac{2}{k_C Q} \cdot \left(1 + \frac{k_C^2}{\beta}\right)} \quad (29)$$

The theoretical maximum achievable efficiency of the *LCLC*-compensated network is shown in Fig. 15, as a function of  $Q$ ,  $k_C$ , and  $\beta$ . It can be seen that the efficiency increases with increasing values of these parameters.

It is informative to compare the efficiencies of the *LC*- and *LCLC*-compensated CPT networks with the same capacitive coupler and the same power level. In the comparison, the coupling coefficients of the *LC*-compensated and *LC*-compensated

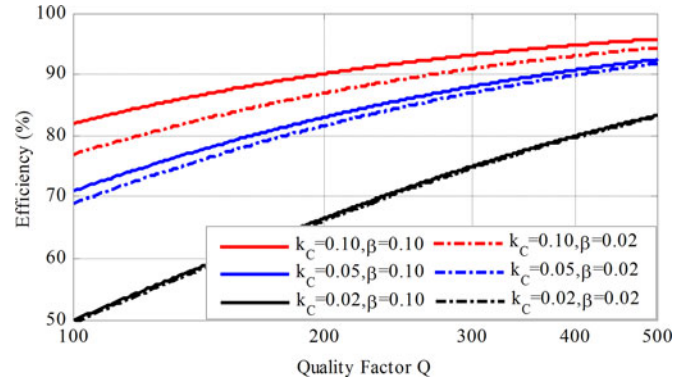


Fig. 15. Theoretical maximum achievable efficiency of a double-sided *LCLC*-compensated CPT network.

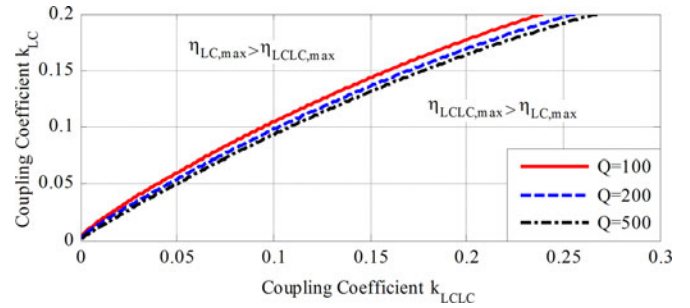


Fig. 16. Comparison of efficiencies of *LC*- and *LCLC*-compensation systems.

networks are defined as  $k_{LC}$  and  $k_{LCLC}$ , respectively. According to the power equations in (14), the value of  $k_{LC}$  must be set equal to the value of  $\beta$  in the *LCLC* system to achieve equal power. Therefore, based on (21) and (29), the optimum efficiency of the *LC*-compensated system is less than that of the *LCLC*-compensated system (i.e.  $\eta_{LC,max} < \eta_{LCLC,max}$ ) when

$$k_{LCLC}^2 - \left( \frac{1}{k_{LC}Q} + \sqrt{1 + \frac{1}{k_{LC}Q}} \right) \cdot k_{LCLC} + k_{LC} < 0. \quad (30)$$

Based on (30), the efficiencies of the *LC*- and *LCLC*-compensated CPT networks are compared in Fig. 16. The area between the curves and the  $x$ -axis is the region where the *LCLC*-compensated system has higher efficiency, and the area between the curves and the  $y$ -axis is the region where the *LC*-compensated system has higher efficiency.

The capacitive coupler designed in Section V can be used to compare the efficiencies of the *LC*- and *LCLC*-compensated CPT networks. In this analysis, the input and output dc voltages are set to 60 V, the switching frequency is set to 1.5 MHz, and the quality factors of the system resonances are assumed to be 400.

Fig. 17 shows the efficiencies of the two networks as a function of power level. The *LCLC*-compensated network results are provided for  $k_{LCLC} = 0.02$  and  $k_{LCLC} = 0.05$ . It can be seen that the efficiencies are relatively independent of power level. In the case of the *LC*-compensated network,  $k_{LC}$  must be reduced in order to increase the system power levels, resulting in lower efficiencies. The resulting range of  $k_{LC}$  is [0.015, 0.04] in

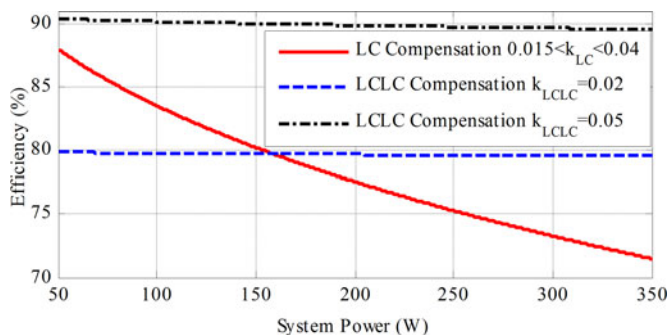


Fig. 17. Efficiencies of *LC*- and *LCLC*-compensated CPT networks using the designed capacitive coupler in Section V.

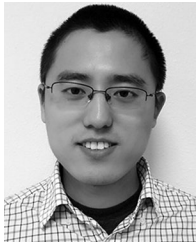
Fig. 17. The results show that the *LC*-compensated CPT system can achieve an efficiency of 80% at 150 W power, not including the inverter and rectifier. When the power electronics circuits are considered, the efficiency agrees with the experimental results in Section V.

## VII. CONCLUSION

This paper proposes a double-sided *LC*-compensation circuit for a loosely coupled CPT system. The frequency properties of the circuit are analyzed, which indicate one CC frequency and two CV frequencies. A prototype of the *LC*-compensated CPT system is designed and implemented to validate the CC and CV working modes. Finally, the *LC* and *LCLC*-compensation topologies are compared in terms of power, frequency properties, and efficiency. It shows that both the *LC*- and *LCLC*-compensated systems can improve efficiency by increasing the coupling coefficient. In a loosely coupled CPT system, the *LCLC* circuit can achieve higher efficiency, as the system power is independent of coupling coefficient.

## REFERENCES

- [1] J. Dai and D. Ludois, "A survey of wireless power transfer and a critical comparison of inductive and capacitive coupling for small gap applications," *IEEE Trans. Power Electron.*, vol. 30, no. 11, pp. 6017–6029, Aug. 2015.
- [2] C. Liu, A. P. Hu, and N. C. Nair, "Modelling and analysis of a capacitively coupled contactless power transfer system," *IET Power Electron.*, vol. 4, no. 7, pp. 808–815, 2011.
- [3] S. Li and C. Mi, "Wireless power transfer for electric vehicle applications," *IEEE J. Emerg. Selec. Top. Power Electr.*, vol. 3, no. 1, pp. 4–17, Mar. 2015.
- [4] F. Lu, H. Zhang, H. Hofmann, and C. Mi, "A high efficiency 3.3 kW loosely-coupled wireless power transfer system without magnetic material," in *Proc. IEEE Energy Convers. Congr. Expo.*, 2015, pp. 2282–2286.
- [5] M. E. Karagozler, S. C. Goldstein, and D. S. Ricketts, "Analysis and modeling of capacitive power transfer in microsystems," *IEEE Trans. Circuit Syst. I, Regul. Papers*, vol. 59, no. 7, pp. 1557–1566, Jul. 2012.
- [6] R. Jegadeesan, Y. X. Guo, and M. Je, "Electric near-filed coupling for wireless power transfer in biomedical applications," in *Proc. IEEE Int. Microw. Workshop Ser. Biomed. Healthcare Appl.*, 2013.
- [7] E. Culurciello and A. G. Andreou, "Capacitive coupling of data and power for 3D silicon-on-insulator VLSI," in *Proc. IEEE Int. Symp. Circuits Syst.*, 2005, pp. 4142–4245.
- [8] D. Shmilovitz, S. Ozeri, and M. Ehsani, "A resonant LED driver with capacitive power transfer," in *Proc. IEEE Appl. Power Electr. Conf.*, 2014, pp. 1384–1387.
- [9] D. C. Ludois, J. K. Reed, and K. Hanson, "Capacitive power transfer for rotor field current in synchronous machines," *IEEE Trans. Power Electron.*, vol. 27, no. 11, pp. 4638–4645, Nov. 2012.
- [10] A. Z. Amanci, H. E. Ruda, and F. P. Dawson, "Galvanic isolation for high frequency applications using an integrated dielectric structure," *IEEE Trans. Power Electron.*, vol. 31, no. 8, pp. 5797–5804, Aug. 2016.
- [11] B. Ge, D. C. Ludois, and R. Perez, "The use of dielectric coatings in capacitive power transfer systems," in *Proc. IEEE Energy Convers. Congr. Expo.*, 2014, pp. 2193–2199.
- [12] J. Dai and D. C. Ludois, "Capacitive power transfer through a conformal bumper for electric vehicle charging," *IEEE J. Emerg. Selec. Top. Power Electr.*, vol. 4, no. 3, pp. 1015–1025, Sep. 2016, doi: 10.1109/JESTPE.2015.2505622
- [13] A. Kumar, S. Pervaiz, C. K. Chang, S. Korhummel, Z. Popvic, and K. K. Afridi, "Investigation of power transfer density enhancement in large air-gap capacitive wireless power transfer systems," in *Proc. IEEE Wireless Power Transfer Conf.*, 2015, pp. 1–4.
- [14] J. Kim and F. Bien, "Electric field coupling technique of wireless power transfer for electric vehicles," in *Proc. IEEE TENCON Spring Conf.*, 2013, pp. 267–271.
- [15] A. Bartlett and P. Arsenault, "Wireless power for vehicle lightweighting, reducing costs, and improving manufacturing efficiencies," in *Proc. IEEE Vehicle Technol. Conf.*, 2015, pp. 1–5.
- [16] A. Sepahvand, A. Kumar, K. Afridi, and D. Maksimovic, "High power transfer density and high efficiency 100 MHz capacitive wireless power transfer system," in *Proc. IEEE Control Model. Power Electron.*, 2015, pp. 1–4.
- [17] L. Huang, A. P. Hu, A. Swain, and X. Dai, "Comparison of two high frequency converters for capacitive power transfer," in *Proc. IEEE Energy Convers. Congr. Expo.*, pp. 5437–5443, 2014.
- [18] B. H. Choi, D. T. Nguyen, S. J. Yoo, J. H. Kim, and C. T. Rim, "A novel source-side monitored capacitive power transfer system for contactless mobile charger using class-E converter," in *Proc. IEEE Vehicle Technol. Conf.*, 2014, pp. 1–5.
- [19] C. K. Chang, G. G. Silva, A. Kumar, S. Pervaiz, and K. K. Afridi, "30 W capacitive wireless power transfer system with 5.8 pF coupling capacitance," in *Proc. IEEE Wireless Power Transfer Conf.*, 2015, pp. 1–4.
- [20] M. P. Theodoridis, "Effective capacitive power transfer," *IEEE Trans. Power Electron.*, vol. 27, no. 12, pp. 4906–4913, Dec. 2012.
- [21] F. Lu, H. Zhang, H. Hofmann, and C. Mi, "A double-sided *LCLC*-compensated capacitive power transfer system for electric vehicle charging," *IEEE Trans. Power Electron.*, vol. 30, no. 11, pp. 6011–6014, Nov. 2015.
- [22] H. Zhang, F. Lu, H. Hofmann, W. Liu, and C. Mi, "A four-plate compact capacitive coupler design and *LCL*-compensated topology for capacitive power transfer in electric vehicle charging application," *IEEE Trans. Power Electron.*, vol. 31, no. 12, pp. 8541–8551, Dec. 2016.
- [23] F. Lu, H. Zhang, H. Hofmann, and C. Mi, "An inductive and capacitive combined wireless power transfer system with *LC*-compensated topology," *IEEE Trans. Power Electron.*, vol. 31, no. 12, pp. 8471–8482, Dec. 2016 doi: 10.1109/TPPEL.2016.2519903.
- [24] F. Lu, H. Zhang, H. Hofmann, and C. Mi, "A *CLLC*-compensated high power and large air-gap capacitive power transfer system for electric vehicle charging applications," in *Proc. IEEE Appl. Power Electr. Conf.*, 2016, pp. 1721–1725.
- [25] F. Lu, H. Zhang, H. Hofmann, and C. Mi, "A loosely coupled capacitive power transfer system with *LC* compensation circuit topology," in *Proc. IEEE Energy Convers. Congr. Expo.*, 2016, pp. 1–5.
- [26] M. kusunoki, D. Obara, and M. Masuda, "Wireless power transfer via electric field resonance coupling," in *Proc. IEEE Asia-Pacific Microw. Conf.*, 2014, pp. 1360–1362.
- [27] R. D. Fernandes, J. N. Matos, and N. B. Carvalho, "Wireless power transmission based on resonant electrical coupling," in *Proc. IEEE European Microw. Conf.*, 2014, pp. 17–20.
- [28] T. Komaru and H. Akita, "Positional characteristics of capacitive power transfer as a resonance coupling system," in *Proc. IEEE Wireless Power Transfer Conf.*, 2013, pp. 218–221.
- [29] Z. Huang, S. Wong, and C. K. Tse, "Design methodology of a series-series inductive power transfer system for electric vehicle battery charger application," in *Proc. IEEE Energy Convers. Congr. Expo.*, 2014, pp. 1778–1782.
- [30] IEEE Standard for Safety Levels with Respect to Human Exposure to Radio Frequency Electromagnetic Fields, 3kHz to 300 GHz, C95.1, 2005.
- [31] S. Li, Z. Liu, H. Zhao, L. Zhu, and Z. Chen, "Wireless power transfer by electric field resonance and its application in dynamic charging," *IEEE Trans. Ind. Electron.*, vol. 63, no. 10, pp. 6602–6612, Oct. 2016.



**Fei Lu** (S'12) received the B.S. and M.S. degree in electrical engineering from Harbin Institute of Technology, Harbin, China, in 2010 and 2012, respectively. He is currently working toward the Ph.D. degree in electrical engineering from the University of Michigan, Ann Arbor, MI, USA.

He is working on the high-power and high-efficiency capacitive power transfer through an air-gap distance up to 100s of millimeters. He is also working on the application of wide bandgap devices on WPT system. His research interests include wireless power transfer for the application of electric vehicle charging.



**Hua Zhang** (S'14) received the B.S. and M.S. degrees in electrical engineering from Northwestern Polytechnical University, Xi'an, China, in 2011 and 2014, respectively. She is currently working toward the Ph.D. degree in electrical engineering from the Northwestern Polytechnical University, Xi'an, China.

From September 2014 to August 2015, she was a joint Ph.D. student funded by the China Scholarship Council with the University of Michigan, Dearborn. In September 2015, she was at the San Diego State

University. Her current research focuses on the coupler design of high-power IPT and CPT system.



**Heath Hofmann** (M'89–SM'15) received the B.S. degree in electrical engineering from The University of Texas at Austin, Austin, TX, USA, in 1992, and the M.S. and Ph.D. degrees in electrical engineering and computer science from the University of California, Berkeley, Berkeley, CA, USA, in 1997 and 1998, respectively.

He is currently an Associate Professor at the University of Michigan, Ann Arbor, MI, USA. His research interests include the design, analysis, and control of electromechanical systems, and power electronics.



**Chunting Chris Mi** (S'00–A'01–M'01–SM'03–F'12) received the B.S.E.E. and M.S.E.E. degrees from Northwestern Polytechnical University, Xi'an, China, and the Ph.D. degree from the University of Toronto, Toronto, Ontario, Canada, in 1985, 1988, and 2001, respectively, all in electrical engineering.

He is currently a Professor and Chair of electrical and computer engineering and the Director of the Department of Energy—funded Graduate Automotive Technology Education Center for Electric Drive Transportation, San Diego State University (SDSU),

San Diego, CA, USA. He is also the Co-Founder of Gannon Motors and Controls LLC, Canton, MI, USA and Mia Motors, Inc, Dearborn, MI, USA. From 2001 to 2015, prior to joining SDSU, he was at the University of Michigan, Dearborn, MI, USA. From 2008 to 2011, he was the President and the Chief Technical Officer of 1Power Solutions, Inc.. He has conducted extensive research and has published more than 100 journal papers. He has taught tutorials and seminars on the subject of HEVs/PHEVs for the Society of Automotive Engineers (SAE), the IEEE, workshops sponsored by the National Science Foundation, and the National Society of Professional Engineers. He has delivered courses to major automotive OEMs and suppliers, including GM, Ford, Chrysler, Honda, Hyundai, Tyco Electronics, A&D Technology, Johnson Controls, Quantum Technology, Delphi, and the European Ph.D School. He has offered tutorials in many countries, including the U.S., China, South Korea, Singapore, Italy, France, and Mexico. He has published more than 100 articles and delivered 30 invited talks and keynote speeches. He has also served as a Panelist in major IEEE and SAE conferences. His research interests include electric drives, power electronics, electric machines, renewable-energy systems, and electrical and hybrid vehicles.

Dr. Mi is received the “Distinguished Teaching Award” and “Distinguished Research Award” of University of Michigan Dearborn, the 2007 IEEE Region 4 “Outstanding Engineer Award,” “IEEE Southeastern Michigan Section Outstanding Professional Award,” and the “SAE Environmental Excellence in Transportation (E2T).”